Materials Chemistry and Physics 297 (2023) 127328

Contents lists available at ScienceDirect

Materials Chemistry and Physics

journal homepage: www.elsevier.com/locate/matchemphys

Grain structure orientational change in Ti6Al4V alloys induced by sea water quenching and novel stress relief annealing process

Amogelang S. Bolokang [a,b,c,*], Maria N. Mathabathe [a], David E. Motaung [c], Christopher J. Arendse [b], Hendrik C. Swart [c]

[a] Council for Scientific Industrial Research, Materials Science and Manufacturing, Light Metals, Meiring Naude Road, P O Box 395, Pretoria, South Africa
[b] Department of Physics, University of the Western Cape, Private Bag X 17, Bellville, 7535, South Africa
[c] Department of Physics, University of the Free State, P.O. Box 339, Bloemfontein, ZA9300, South Africa

HIGHLIGHTS

- Sea water quenching induced novel microstructures in Ti6Al4V alloys.
- Annealing at 900 °C induced thermal shock with increased hardness.
- Equiaxed grains was developed on alloys quenched at 1000 °C after annealing.
- EBSD analysis revealed the recrystallization of β-Ti phase on 1100 °C alloys.

ARTICLE INFO

Keywords:
Ti6Al4V alloy
Grain orientation
Sea water quenching
EBSD
Microstructure

ABSTRACT

We report on the microstructures and properties of Ti6Al4V alloys, which were achieved upon quenching in sea water medium with potential high cooling rate. The Ti6Al4V alloys were quenched at 1000 and 1100 °C, respectively. Moreover, the effect of post-quenching annealing performed at 900 °C was analyzed. As a result, the quenched alloy experienced surface thermal stress, due to rapid cooling and thermal shock, due to exposure to high temperature annealing. The alloy quenched at 1000 °C developed equiaxed grain structure after annealing, while the 1100 °C-quenched alloy generated irregular shaped lamellae structures. TEM analysis for the 1000 °C-quenched samples revealed the α′-martensite decomposed into the equilibrium α + β phases. Moreover, the 1100 °C-quenched Ti6Al4V alloy revealed an α′-acicular martensitic structure.

1. Introduction

Heat treatment of metallic materials is a common process of improving metal and alloy's mechanical properties. These processes are annealing (furnace cooling), normalizing (air cooling), spheriodizing, quenching and tempering (stress relief after quenching), whereby the quenching solutions are differentiated by their respective cooling rates. These methods, which are commonly used in steels, aluminium and titanium alloys are instrumental in altering alloys microstructures. Titanium (Ti) alloys reveals the interesting microstructures composed of martensitic laths injected with novel properties [1–5]. These features are inherited in a pure Ti with a hexagonal close packed (HCP) structure, which transforms upon heating above 882 °C and changes to body-centred cubic (BCC) structure. When cooled down to room temperature, this metal remembers its ground state HCP crystal structure; and this phenomenon called the (α↔β) reversible phase transformation [6,7]. This α↔β phase transition temperature can be altered by impurities, alloying as well as deformations processes [7,8]. Quenching from high temperatures and annealing of commercial pure (CP) Ti result in improved corrosion properties by rearranging grains in a precise direction [9]. The multiple steps involving high-temperature cycles during heat treatment may result in a mixture of crystal orientations and yield mechanical properties, which are different from the original processing [10]. Among Ti alloys, the Ti6Al4V is an important alloy comprising high strength, low density, and good corrosion resistance. It is used in aerospace, biomedical, marine, and other important structural

* Corresponding author. Council for Scientific Industrial Research, Materials Science and Manufacturing, Light Metals, Meiring Naude Road, P O Box 395, Pretoria, South Africa.
E-mail addresses: sbolokang@csir.co.za, bolokang.sylvester@yahoo.co.uk (A.S. Bolokang).

https://doi.org/10.1016/j.matchemphys.2023.127328
Received 7 November 2021; Received in revised form 17 December 2022; Accepted 3 January 2023
Available online 9 January 2023

Table 1
Chemical composition of Ti–6Al–4V ELI.

Al	V	Fe	H	C	W	O	Ti
5.96	3.98	<0.275	≤0.01	≤0.079		≤0.2	balance

applications. Recently, additive manufacturing (AM) has attracted research interest, due to evolution in development in novel microstructures [11]. This process induces microstructures but slightly different from the normal conventional quenching, while all induce metastable phases. The AM rapid cooling is due to thin layer deposition during the material built-up. AM capabilities include the ability to build intricate shaped biomedical Ti6Al4V products, which are usually difficult to produce by other manufacturing processes, such as casting [12], products with controlled porosity [13,14] and surface modifications [15]. However, heat treatment of the as-cast products is still a competitive process especially with further processing. For example, on the microstructure of Hot Rolled Ti–6Al–6Nb Alloy, reduction of elastic modulus to 106 GPA for medical application was realised [16]. The quenching process improves mechanical properties and alters materials microstructure [17–21]. The final desired microstructure with induced properties is dependent on the cooling rates and post heat treatment as to release the quenching stresses. The traditional post heat treatment reduces materials hardness. For the first time in this paper, we report on novel microstructure with improved hardness upon post heat treatment of the Ti6Al4V alloy quenched in sea water. These novel properties were achieved by returning the alloy into the hot furnace at the β-zone temperatures without inducing any quenching cracks on the material. To the best of our knowledge, this work is reported for the first time in this study.

2. Experimental procedure

The Ti6Al4V cylindrical ingot with a chemical composition and diameter of 70 mm was used for this work, as detailed in Table 1. The ingot was sectioned into 12 samples, with a 5 mm in thickness. The heat treatment cycles were conducted on six samples at 1000 °C and other six samples at 1100 °C in a tube furnace operated with ±10 °C error for 2 h (h). The samples were further quenched in sea water. Three quenched samples from 1000 °C to 1100 °C were annealed in a furnace operating at 900 °C and allowed to cool steadily at 20°/min. The schematic representation of the experimental process is shown in Fig. 1. Metallographic examinations were performed on heat-treated specimens by grinding with silica papers and polishing in colloidal silica.

2.1. Characterization

High-resolution scanning electron microscope (HR-SEM, Auriga ZEISS) coupled with a Robinson Backscatter Electron Detector and an Oxford Link Pentafet energy-dispersive x-ray spectroscopy (EDS) detector was used to analyze microstructures of the Ti6Al4V samples. The four samples analyzed for electron backscatter diffraction (EBSD) analyses were polished up to colloidal silica and electro-polished. The specimens were investigated for diffraction patterns, and orientation determination, which consisted of 1, Kikuchi band detection, 2, Kikuchi band identification, and indexing of pattern, 3, determination of orientation. These analyses were based on calculation of the orientation of the corresponding crystal lattice with respect to reference frame, and the crystal orientation, which is defined by three Euler angles (φ1, φ, φ2) Stojakovic [22]. Therefore, this is a representation of successive conventional rotations to match the crystal orientation with a Cartesian coordinate system related with the sample surface [22]. Further analysis of the microstructures was investigated by the high-resolution transmission electron microscopy (HR-TEM) and selected area electron diffraction (SAED). Thin foil specimens were ground to the thickness of 100 μm for TEM observations using twin-jet electropolishing with a solution of 6 vol% $HClO_4$ + 34 vol% C_4H_9OH + 60 vol% CH_3OH. The temperature of the electrolytic bath was maintained below −30 °C under a voltage of 30V to prevent hydrogen pick-up during electropolishing.

The structural changes in the alloys were probed using a PANalytical X'pert PRO PW 3040/60 X-ray diffraction (XRD) machine, using Cu K_α radiation as a source. The hardness measurements of the polished specimens were performed according to the requirements of ASTM standards E384-11. Micro-Vickers hardness (HV) measurements were performed at an applied load of 500 g/f and dwelling time of 10s. Hardness profiles throughout the specimens were measured at an average of at least 10 measurements. The bulk oxygen (O) content of the

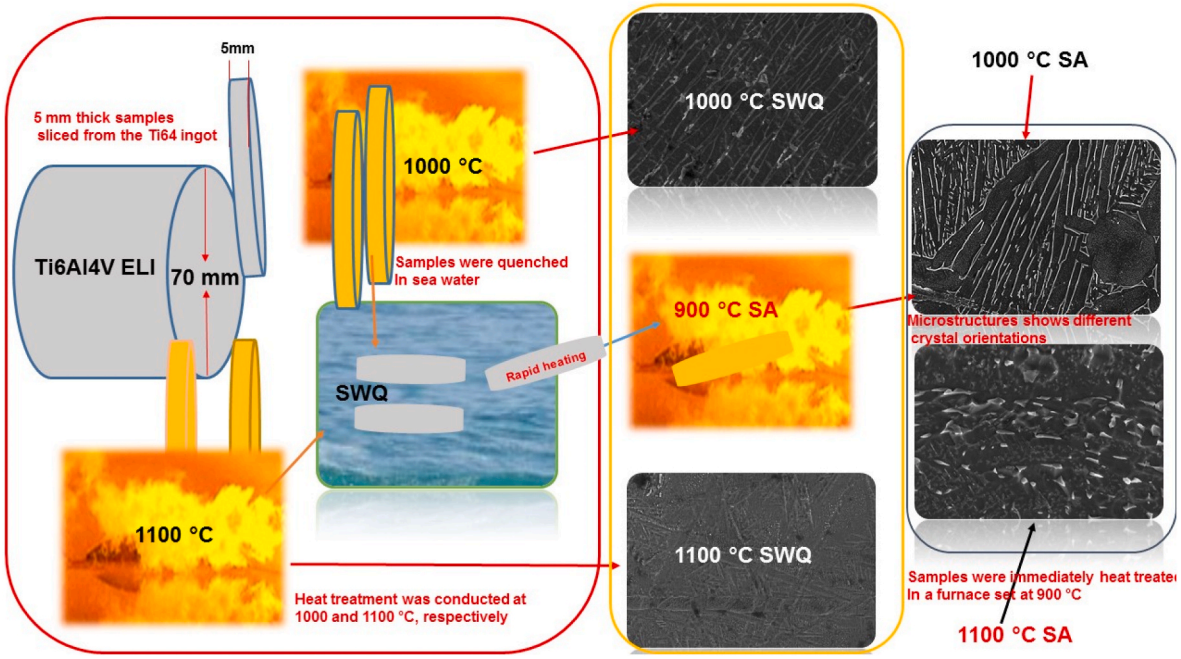

Fig. 1. Schematic illustration of the experimental work on heat-treated Ti–6Al–4V samples.

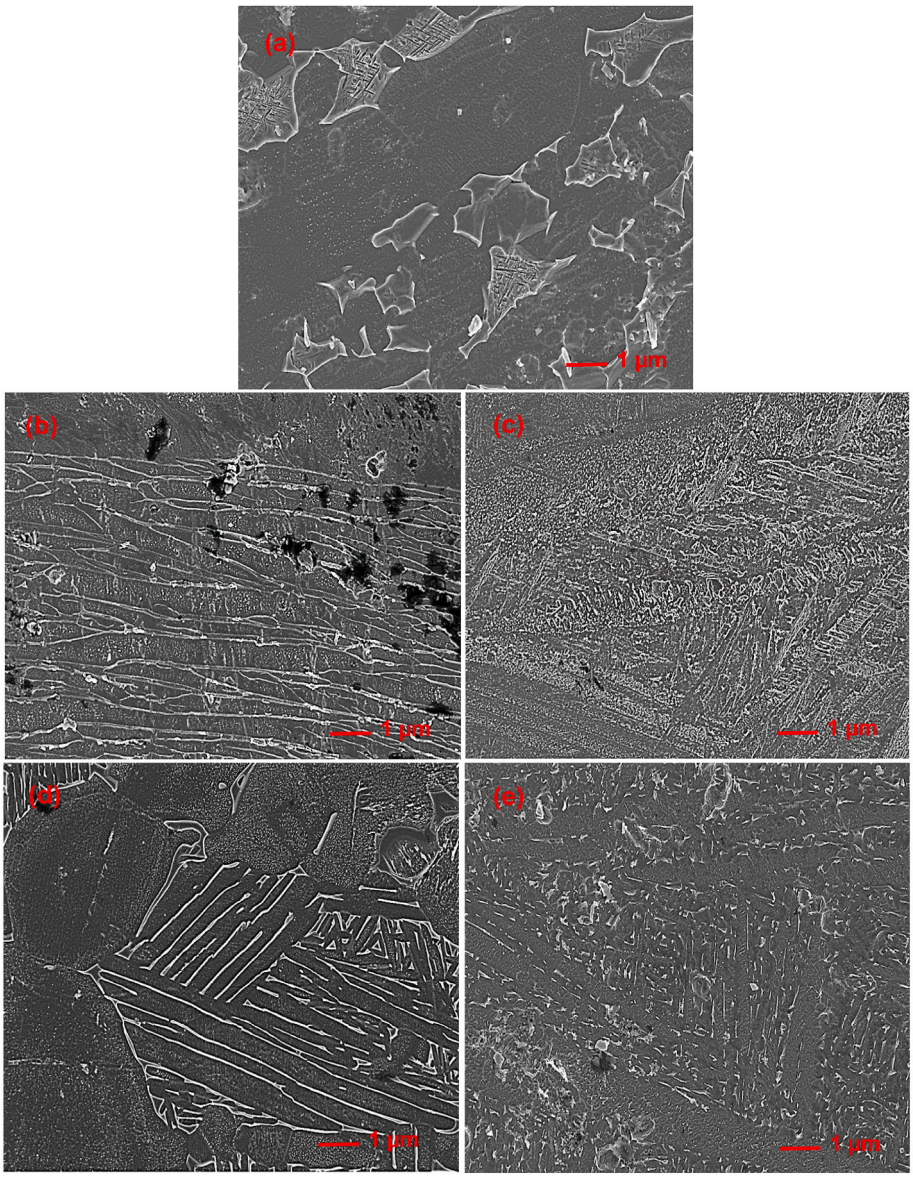

Fig. 2. SEM images of the (a) as-cast, (b) 1000 °C-quenched, (c) 1100 °C-quenched, (d) 1000 °C and (e) 1100 °C Ti6Al4V alloys annealed after quenching.

Ti6Al4V alloys was determined by means of ELTRA ONH 2000 PC under Helium gas atmosphere.

3. Results and discussions

Fig. 2a shows the microstructure of the sectioned samples of Ti6Al4V ingot. They comprised of α' (dark) and β (light)-phases. Due to quenching at 1000 °C in sea water, formations of α and α′-lamellae were observed. The resultant microstructure resembled a fishbone martensitic lath with irregular-shaped dark dots attributed to partial oxidation on the materials (Fig. 2b). The partial oxidation was justified by oxygen content measured on the alloys. The as-received alloy composed of 0.113 wt% oxygen. Upon quenching at 1000 °C, the oxygen content slightly increased to 0.173 wt%. While after stress relief annealing the quenched sample, it increased to 0.217 wt%. Similarly, the 0.132 wt% was obtained after quenching at 1100 °C and increased to 0.191 wt% upon stress relief annealing. The sample quenched at 1100 °C (Fig. 2c) revealed ultrafine laths with fishbone type martensite. Upon stress-relief annealing at 900 °C, the 1000 °C quenched alloy (Fig. 2d), formed equiaxed grains with lamellae oriented in different directions [23]. These quenched microstructures (1000 °C and 1100 °C) formed due to high cooling rates provided by quenching in sea water. The stress relieved 1100 °C sample (Fig. 2e) was also annealed at 900 °C.

Reports on molecular dynamics studies showed that the twin boundaries suppress the dislocation motion, which result in material's strengthening [24]. It is important to note that the theoretical density of a sample can be calculated using the rule of mixtures employing volume

Table 2
XRD analysis of the as-cast, 1000 °C-quenched, 1100 °C-quenched, 1000 °C and 1100 °C annealed after quenching Ti6Al4V alloys.

Sample ID	Crystal structure	a	b	c	c/a
As-received	HCP	5.7410		4.6306	0.8066
Q-1000 °C	HCP	2.9200		4.6200	1.5822
	HCP	5.8450		4.6700	0.7989
SA-1000 °C	HCP	2.9200		4.6700	1.5993
	FCC	4.0699			
Q-1100 °C	Monoclinic	4.4566	3.0022	4.4760	1.0044
	HCP	2.9400		4.7200	1.6054
SA-1000 °C	HCP	2.9020		4.7340	1.6313
	HCP	2.8870		4.6750	1.6193
	Monoclinic	4.0614	6.4476	2.6582	0.6545

Table 3
Theoretical density of raw powders.

Elemental powders	Theoretical density (g/cm^3)	Supplier
Ti–6Al–4V (pre-alloyed)	4.43	AP&C (MSDS)
CP Ti (HCP)	4.5	Sigma-Aldrich
Al (FCC)	2.7	TLS Technik GmbH & Co
V (BCC)	6.11	Alfar Aesar

fractions of elements Eq. (1) [25].

$$p_{theoretical} = \frac{m}{V_{SOLID} + V_{EP}} \quad (1)$$

where m is the mass of the powders, V_{solid} is the solid volume, and V_{ep} is the entrapped pore volume. Table 3 shows theoretical density of each elemental powders, which may have a variable ratio out of the 6Al–4V alloy specification. The bulk Ti–6Al–4V alloy ingot is an HCP structure, meanwhile, the collated monoclinic structure in Table 2 and Fig. 4d was ascribed to oxygen adsorption during annealing processes. Oxygen has high affinity for Vanadium, and only its selective amount is required to form vanadium oxide (V_2O_5). This oxide exhibits a monoclinic crystal structure (non-conductive, M-phase) at room temperature, and transform to a tetragonal phase (conductive, R-phase) above 68 °C [26].

Julien et al. [20], reported Ti–6Al–4V tempered at 730 °C, after quenching it resulted in β-phase transformation to lamellar structure consisting of colonies of secondary α in the β-phase. Similarly, in the current work, duplex microstructure was obtained. It is evident that the cooling rate greatly influenced the microstructure [20]. Similar alloys, such as TC21 (Ti–6Al–2Sn–2Zr–3Mo–1Cr–2Nb–Si wt.%) has secondary α-phase precipitated in residual β-phase due to the step cooling from 900 to 800 °C during heat treatment [18]. The cooling rates plays an important role in the development of microstructures.

The micro-hardness of the annealed alloys was measured to verify if annealing has induced any dislocations, due to immediate annealing of the sample at 900 °C after quenching. Traditionally, the tempering process makes the as-quenched material softer. In the current work, the tempered Ti6Al4V alloys showed increased hardness, implying that the applied annealing at 900 °C induced surface thermal shock. In the microstructural analysis, it was observed that the 1000 °C quenched sample yielded a low volume of martensite plates in comparison with the 1100 °C quenched samples. On average, the microhardness of the as-received is 317 ± 13 HV, which is comparable to the microhardness of 1000 °C-quenched sample (318 ± 11 HV). Upon annealing at 900 °C the hardness was increased to 333 ± 13 HV. While at 1100 °C, the hardness of the as-quenched was 368 ± 13 HV, which increased to 379 ± 09 HV after annealing. Since annealing was conducted above the allotropic α↔β reversible phase transformations temperature of pure Ti [27], this behaviour was attributed to the β-phase precipitation. For example, CP Ti has HCP (α) crystal structure, which transforms to body-centred cubic (β) crystal structure (α→β) starting at ~883 °C, a reversible transition (β→α) upon cooling. When rapid cooling is introduced, Ti eludes this thermodynamic rule at the expense of forming metastable phases (high temperature phases at low temperature) and new microstructures with altered crystal orientations and better mechanical properties formed [21,28]. The microstructures of Ti-based alloys offer martensitic transformation with distinguished plates, lamellae, or needles. Heat treatment and alloying elements are crucial to the final structure of these Ti alloys. For example, Mathabathe et al. [5], reported high-temperature reversible transition in Ti-(45–48) Al alloy and martensitic plates with improved mechanical properties. In this work, Ti6Al4V alloys were quenched in sea water where the interfacial strain from the β-region facilitated microstructural change [27]. The grain boundary ratio of the annealed alloy is larger than that of the quenched alloy, as shown by the equiaxed and the triangular grains, respectively. Grain boundaries are barriers to slip and increases with misorientation. On the other hand, smaller grain size are barriers to slip. The quenched alloy with relatively larger grain sizes than the tempered annealed alloy can have more dislocation pile up, leading to a bigger driving force for dislocations to move from one grain to another. As a result, less force is required to move a dislocation from a larger grain, than from a smaller grain. Materials with smaller grains exhibit higher yield stress, hence, our annealed alloys have higher hardness, due to induced surface thermal stress compared to the quenched alloy, this agrees with the Hall Petch relation, which indicates that the yield strength has an inverse square root relation with the grain size [22]. The stress required to move dislocations from one grain to another, to plastically deform a material depends on the grain size. Solid metals expand when heated to high temperature, since material volume increase and decrease when cooled [28]. The difference in the coefficient of thermal expansion at high temperature generates internal stresses at the α/β interface weakening the interface bonding strength [29]. The α-region in CP Ti has thermal expansion (α) of ~8.4 × $10^{-6}C^{-1}$ while the β-phase is larger (~9.7 × $10^{-6}C^{-1}$) [30]. In Ti6Al4V alloy, several authors measured the α to be ~5.5–8.6 × $10^{-6}C^{-1}$ [31–33]. Sun et al. [34], reported a larger thermal expansion of 9.2 × $10^{-6}C^{-1}$ for Ti6Al4V alloy. Rapid cooling induces residual stresses which requires stress relief heat treatment depending on the manufacturing processes [35–38], such as laser deposition on material surfaces [39–41]. Sea water has superior cooling rates than normal water since it prevents the formation of the stable film after

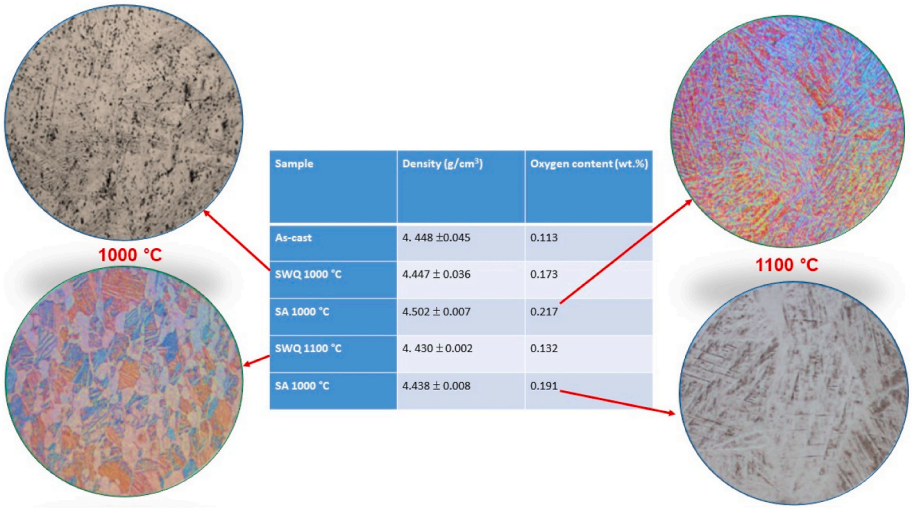

Fig. 3. Density, oxygen analysis and optical microstructures of the quenched and post-quenched annealing of Ti6Al4V alloys.

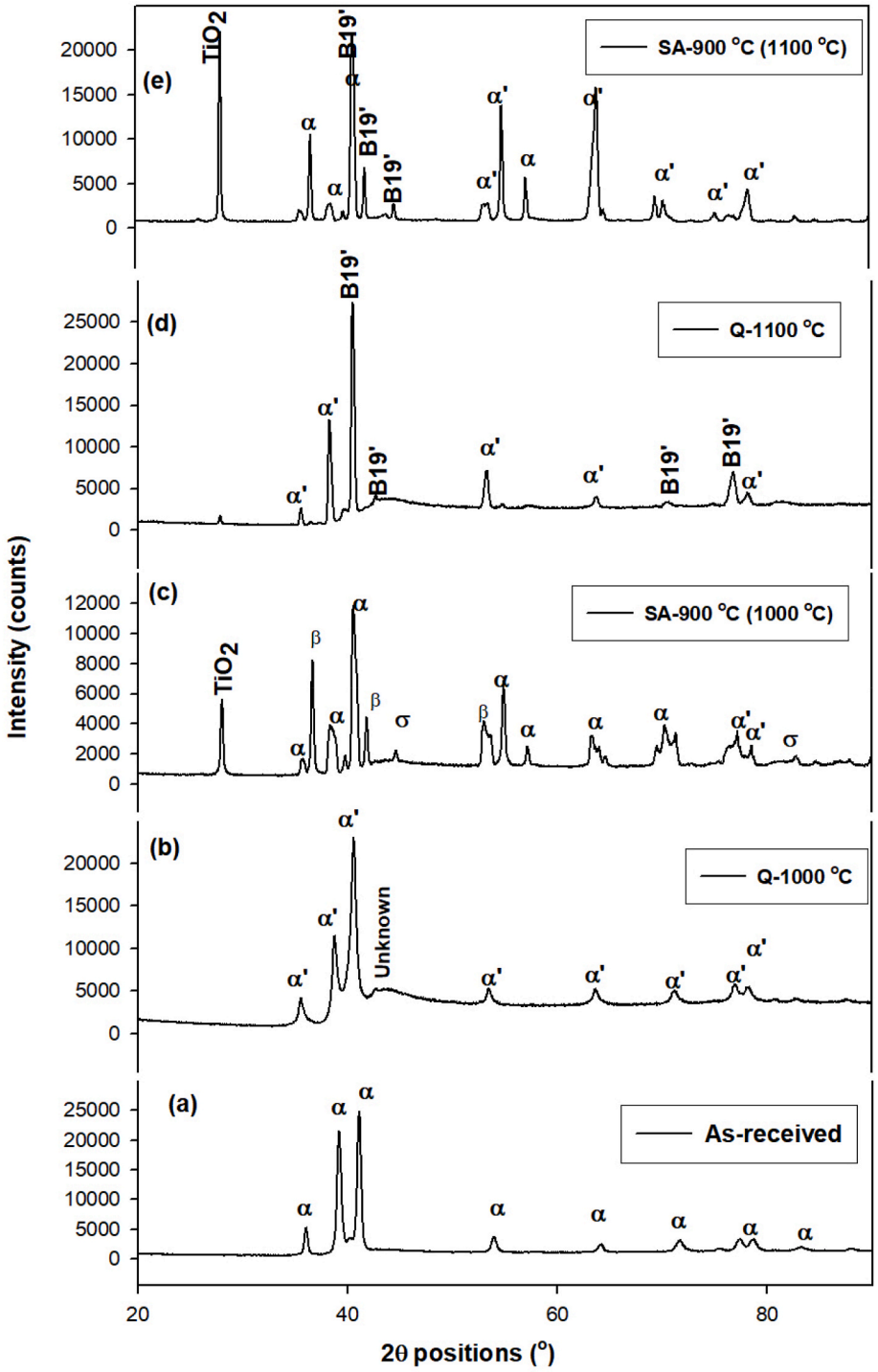

Fig. 4. XRD patterns of the Ti6Al4V alloys (a) as-cast, quenched alloys at (b) 1000 °C, (c) 1100 °C, annealing after quenching of (d) 1000 °C and (e) 1100 °C at 900 °C.

boiling [42]. It enables much more rapid quenching through the prevention of stable film boiling, due to a zeta-potential effect. The quenching starts with transition boiling characterized with moderate bubble nucleation sites and possible burst out of bubble clusters [42]. It has been established that the interfacial temperature of the alloy conducted in sea water at 1000 °C is approximately 100 °C or less [42]. Therefore, the Ti6Al4V quenched at 1000 °C means the interfacial temperature occurred almost at the α/β-zone (~900 °C), while quenching at 1100 °C safely occurred in the β-region (1000 °C). There are obvious variations in mechanical properties between 1000 and 1100 °C quenched samples. It was previously shown that CP Ti quenched from 1000 °C to 1200 °C in pure water produce martensitic plates with different crystal orientations [21]. During quenching, the cubic symmetry of the β-phase breaks into martensitic variants of the metastable phases [43].

Fig. 3 presents the density and oxygen analysis of Ti6Al4V samples annealed and quenched at 1000 °C and 1100 °C-quenched, respectively. The heat treatment effect on the density of Ti6Al4V samples was negligible. The annealed samples after quenching adsorbed oxygen, probably due to exposure to air. After quenching at 1000 °C, oxygen (O)

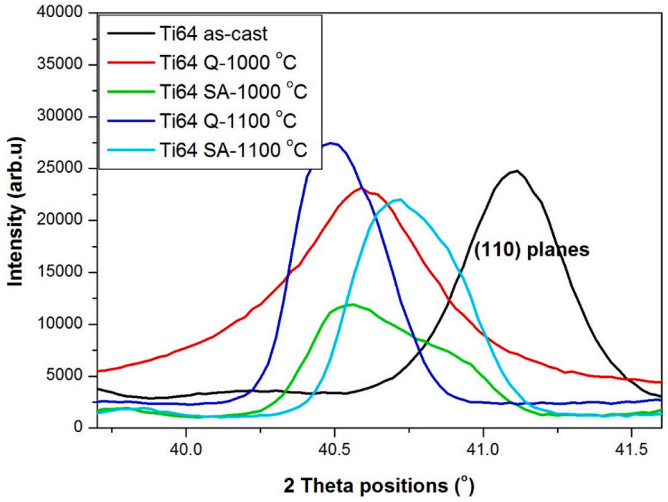

Fig. 5. XRD pattern of the Ti6Al4V alloys focused on the (110) peak of the as-cast, quenched and annealed samples.

content was 0.173 ± 0.11 wt%, and it increased to 0.217 ± 0.15 wt% upon annealing. For quenched samples at 1100 °C, the O content of 0.132 ± 0.09 wt% was measured, which increased to 0.191 ± 0.13 wt% after annealing. This slight increase in O content after annealing was attributed to contamination by air, due to sample handling.

The phase changes of the Ti6Al4V alloys after quenching and annealing were monitored by the XRD technique. Fig. 4a shows the XRD patterns of the Ti6Al4V rod before heat treatment. Pure Ti phase with normal HCP (α) and lattice parameters a = 2.951 Å; c = 4.682 Å with $c/a = 1.587$ was detected, since the Ti6Al4V is Ti rich alloy. Additionally, another α-phase was detected with lattice parameters a = 5.7410 Å; c = 4.6306 Å and $c/a = 0.8066$ Å as displayed in Table 2. The Al addition in Ti6Al4V increased the alloy strength and stability of the α-phase, while the V stabilises the high temperature β-phase. Due to the dominance of pure Ti, the Ti6Al4V alloy inherited the reversible first-order phase transformation [7]. This transition is represented by the endothermic peaks during thermal analysis like the second-order phase transition in ferromagnetic metals [44,45]. This implies that Al and V alloying dictates the phase transformation temperature to confirm the effectiveness of alloying. Fig. 4b shows the XRD patterns of the Ti6Al4V alloy after quenching in sea water at 1000 °C. The alloy yielded two HCP phases with different lattice parameters a = 2.9200 Å; c = 4.6200 Å and a = 5.8450 Å; c = 4.6700 Å. The former resembles the crystal structure closely related to pure Ti with c/a = 1.5822. Upon annealing at 900 °C, more phases were detected by the XRD (Fig. 4c). A single peak of TiO_2 emerged, which was attributable to the increased O content of the sample, as shown in Fig. 3. Moreover, the β-phase with a = 6.920 Å and the FCC with a = 4.0699 Å phase were formed. The FCC phase in Ti6Al4V alloys was previously reported, and it was attributed to deformation and stress in processes, such as HPT [46], High energy shot peening HESP [47], ultrasonic surface rolling process [48]. In the current investigation, the FCC phase is detected with smaller lattice parameter in comparison to Refs. [46–48]. This was attributed to stresses induced by quenching with high cooling rates. Fig. 4d presents the XRD patterns of the Ti6Al4V alloy quenched at 1100 °C in sea water, quenched at ~100 °C above the β-zone. Quenching in water induce

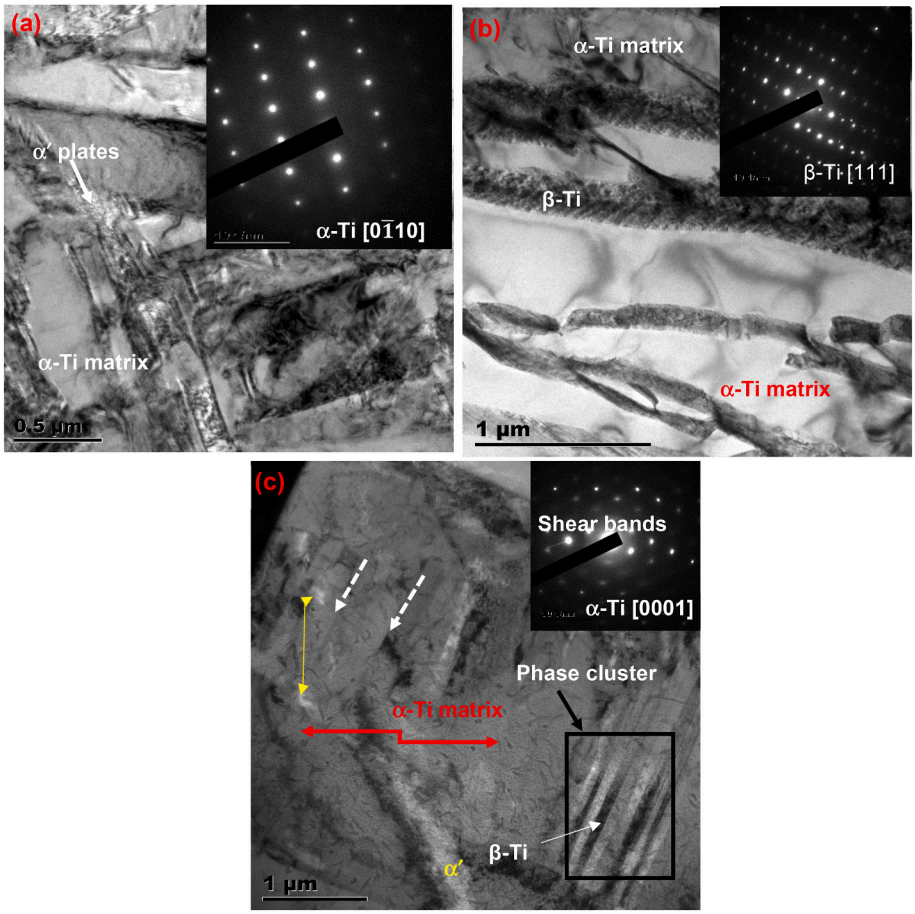

Fig. 6. Bright field transmission electron microscopy (TEM) micrographs of (a) Ti–6Al–4V alloys quenched at 1000 °C and (b) Annealed at 900 °C after quenching at 1000 °C, and at (c) 1100 °C with their corresponding SAED patterns.

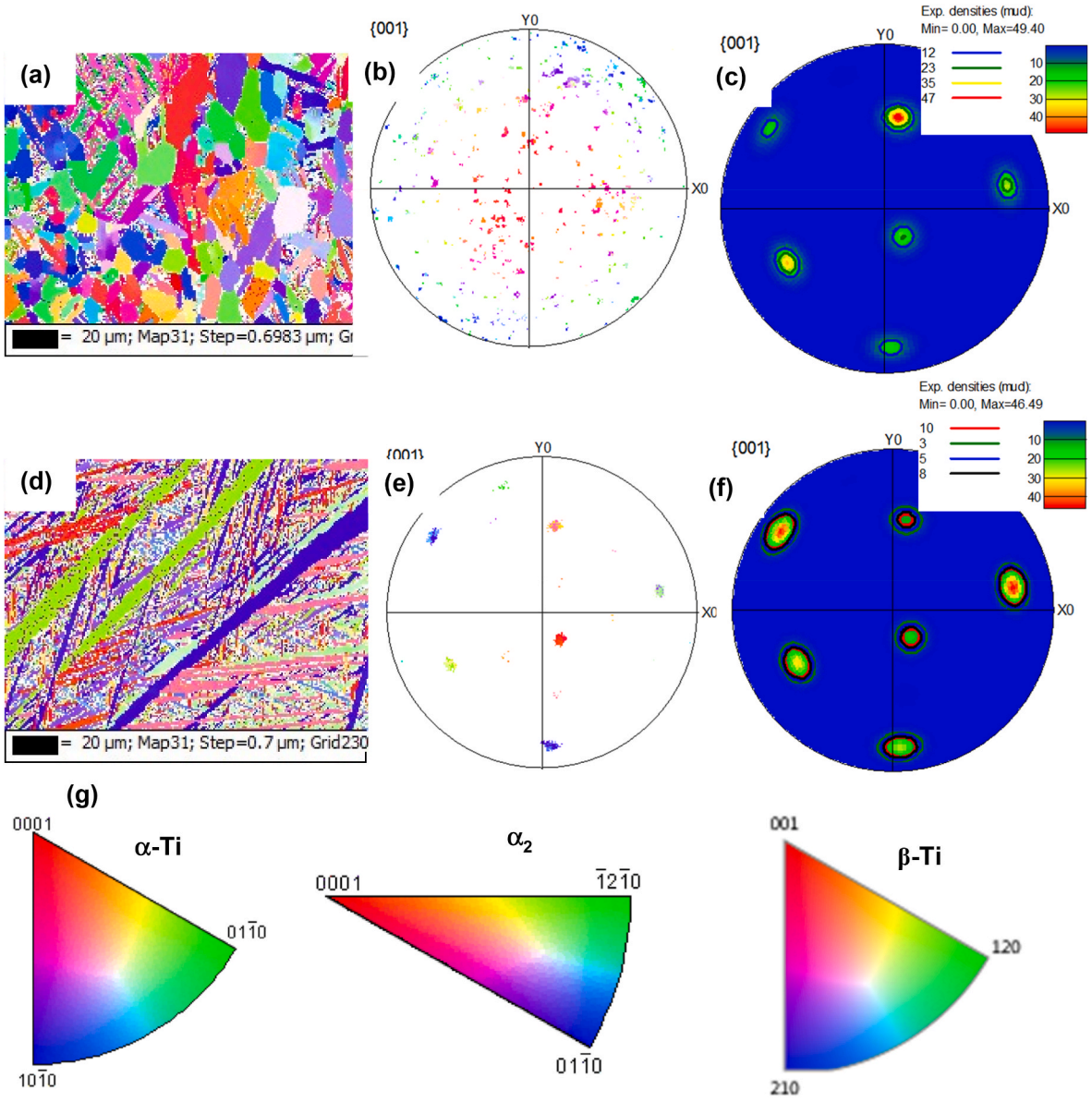

Fig. 7. EBSD inverse pole figure (IPF) maps of the samples annealed after quenching for 1000 °C, and 1100 °C Ti6Al4V alloys.

stresses in the alloy and introduces novel metastable phases, which are not commonly found by slow cooling [21]. The α-phase with a = 2.9400 Å; c = 4.7200 Å and c/a = 1.6054 Å lattice parameters was detected. Furthermore, a monoclinic structure with a = 4.4566 Å; b = 3.0022 Å; c = 4.4760 Å formed attributable to stress induced by high cooling rates. This monoclinic phase is different from the monoclinic phase common in alloys such as TiNi [49]. Upon annealing at 900 °C, two HCP crystal structures and a monoclinic phase with different lattice parameters (a = 4.0614 Å; b = 6.4476 Å; c = 2.6582 Å) were detected. This monoclinic phase was due to oxygen contamination, since this alloy dissolved slightly at higher oxygen after annealing as shown in Fig. 3.

Structural changes in Ti6Al4V alloy due to quenching followed by annealing are shown in Fig. 5. The (110) XRD peak of the Ti6Al4V alloy was examined. The peak shifting due quenching and annealing is evident in Fig. 6. The (110) peak of the as-cast Ti6Al4V alloy is positioned at 41.092°. After quenching at 1000 and 1100 °C, the peaks shifted towards lower angles of 40.568°, 40.484° due to stress induced by rapid cooling. Upon annealing, negligible peak shifts were observed on the sample quenched at 1000 °C and this is in-line with the microhardness of two samples. On contrary, the alloys quenched and annealed at 1100 °C revealed a significant overlapping of peaks, and this is also in agreement with both alloys' microhardness values.

Fig. 6a shows the TEM images of the Ti–6Al–4V alloy after quenching at 1000 °C. It is evident that the α′-martensite has decomposed into equilibrium α + β microstructure. This behaviour was observed by Liu and Shin [15] where the substantial amount of α′-martensite originated from the high built heat treatment temperature. Moreover, this structure produced the diffused-Debye rings as shown from the SAED patterns (inset of Fig. 6a). Similarly, quenching the Ti6Al4V alloy at 1100 °C showed the microstructural features of an α′-acicular martensitic structure, like the α′ network observed in Fig. 6a which is an indication of randomly oriented grains [50].

Fig. 6b shows the bright-field TEM micrograph of the 1000 °C quenched alloy after annealing. The microstructure reveals the β-phase strips along with the α-Ti matrix. These β-strips are ~200–300 nm thick and positioned between the α-Ti grains. The SAED patterns (inset of Fig. 6b) confirms the overlaying of diffraction patterns of both the β-Ti precipitates and the α-Ti matrix. The TEM image of the 1100 °C quenched Ti6Al4V alloy after annealing shows the α′-martensitic plates, β-phase precipitates, and the α-Ti matrix (Fig. 6c). The enrichment in the

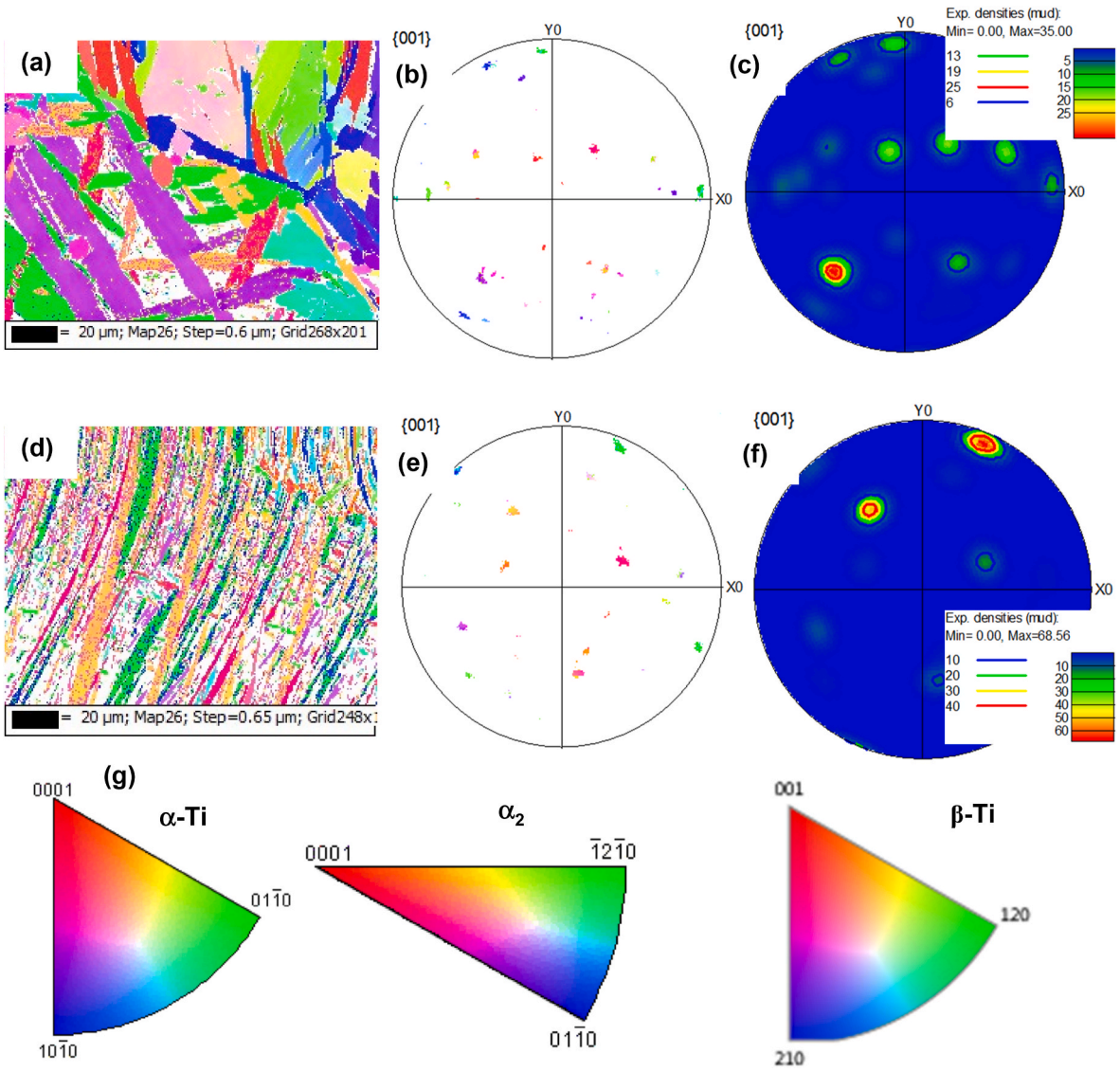

Fig. 8. EBSD inverse pole figure (IPF) maps of the samples quenched at 1000 °C, and 1100 °C Ti6Al4V alloys.

precipitation of α′-phase is highly inclined to be liable for surface/subsurface cracking, as indicated by the shear bands in Fig. 6c. This behaviour implies that annealing on quenched samples has initially introduced surface thermal stresses by shock. The SAED patterns in Fig. 6c (inset) demonstrate an overlay of phase clusters of β/α′ precipitates and the α-Ti matrix.

Figs. 7 and 8 represents the EBSD-IPF maps of the quenched and annealed Ti6Al4V alloys. The inverse pole figure maps in Figs. 7 and 8 indicate that extensive amount of β-Ti phase has recrystallized during annealing. Moreover, the grain orientation of the recrystallized β-Ti grains was virtually random, implying that there was obvious texture. In contrast, the β-Ti crystallographic aspects (texture analysis) for the equiaxed, basketweave, and colonies/laths structures were performed. There is a relationship between the α-laths and the BCC β-matrix, which is known as the Burgers orientation relationship (BOR). The relationship was established on two parallel planes (0001)α || {110}β, and the directions <11 $\bar{2}$ 0>α || <111>β in the several phases [51]. Moreover, there is a possibility that a total number of 12 varying variants of the α/α′ nucleates from the β-matrix [51]. It is important to note that high cooling rate induced by sea water qualifies an adequate amount of driving force for the formation of α′-laths, with nearly all possible variants [51]. This is stipulated by α′-phase fractions increasing with higher cooling rate i.e., annealed sample compared to quenched sample. As a result, the formation of laths with respective various orientations gave rise to a basket weave microstructure. The study on CP Ti showed that microstructural features of most Ti-based alloys entail similar behaviour of pure Ti [21]. Tarzimoghadam et al. [52], conducted a systematic study by avoiding complex ternary and quaternary Ti alloys and studied Ti–4Mo wt% to show that it has a broad variety of microstructure formation mechanisms after heat treatment. In this study, the 1000 °C quenched sample yielded a low volume of martensite plates in comparison with the 1100 °C quenched samples. The EBSD analysis of the Ti6Al4V alloy showed similar behaviour of the α-phase nucleation and growth at the α-grain boundaries or within the α-grains as plates showing variants with one grain [53]. Equiaxed microstructure comprised of randomly distributed lamellar secondary α-phase in equiaxed grains. Thus, we assume that the β-related structure is prompted by the combination of β-stabilizer (V) and the high cooling rates.

4. Conclusions

In summary, microstructures, and properties of Ti6Al4V alloys achieved after quenching in sea water with potential high cooling rate were investigated. The Ti6Al4V alloys were quenched at 1000 and 1100 °C.

The effect annealing the quenched alloys was performed at 900 °C. The annealing of the quenched alloy samples induced surface thermal stress, due to sudden exposure to high temperatures, which resulted in different microstructures with higher hardness values. The 1000 °C-quenched samples revealed an equiaxed grain structure after annealing while the 1100 °C-quenched generated lamellae structure with irregular shaped particles. TEM analysis for the 1000 °C-quenched samples revealed the α′-martensite decomposed into the equilibrium α + β phases. The 1100 °C-quenched Ti6Al4V alloy revealed an α′-acicular martensitic structure. The microstructure exhibited a notable amount of fringe contrast, suggesting favourably dense dislocations pile-up in the microstructure. After annealing the 1000 °C quenched alloy, the β-phase strips formed along with the α-Ti matrix. TEM studies of the alloy quenched at 1100 °C and annealed at 900 °C showed the α′-martensitic plates, β-precipitates, and the α-Ti matrix. The EBSD analyses of inverse pole figure indicated the recrystallization of β-Ti phase upon the post-quenched annealing treatment. A clear relationship between the α-laths and the β-matrix, which is known as the Burgers orientation relationship (BOR) was observed.

CRediT authorship contribution statement

Amogelang S. Bolokang: Conceptualization, Writing – original draft, Writing – review & editing, Formal analysis. **Maria N. Mathabathe:** Data curation, Formal analysis. **David E. Motaung:** Data curation, Formal analysis, Writing – review & editing. **Christopher J. Arendse:** Validation, Writing – review & editing. **Hendrik C. Swart:** Validation, Supervision, Writing – review & editing.

Declaration of competing interest

The authors declare that they have no known competing financial interests or personal relationships that could have appeared to influence the work reported in this paper. There is no conflict of interests for this article.

Data availability

Data will be made available on request.

Acknowledgements

Council for Scientific and Industrial Research is acknowledged for funding this work through the Human Capital Development-Chief Researcher Fund Program.

References

[1] Q.C. Fan, Y. Zhang, Y.H. Zhang, Y.Y. Wang, E.H. Yan, S.K. Huang, Y.H. Wen, Influence of Ni/Ti ratio and Nb addition on martensite transformation behavior of NiTiNb alloys, J. Alloys Compd. 790 (2019) 1167–1176.
[2] H. Yang, D. Wang, X. Zhu, Q. Fan, Dynamic compression-induced twins and martensite and their combined effects on the adiabatic shear behavior in a Ti-8.5Cr-1.5Sn alloy, Mater. Sci. Eng., A 759 (2019) 203–209.
[3] J. Tang, H. Luo, Y. Qi, P. Xu, J. Lv, Y. Ma, Z. Zhang, Effect of nano-scale martensite and b phase on the passive film formation and electrochemical behaviour of Ti-10V-2Fe-3Al alloy in 3.5% NaCl solution, Electrochim. Acta 283 (2018) 1300–1312.
[4] M.N. Mathabathe, A.S. Bolokang, G. Govender, R.J. Mostert, C.W. Siyasiya, Structure-property orientation relationship of a gamma/alpha2/Ti_5Si_3 in as-cast Ti-45Al-2Nb-0.7Cr-0.3Si intermetallic alloy, J. Alloys Compd. 765 (2018) 690–699.
[5] M.N. Mathabathe, S. Govender, A.S. Bolokang, R.J. Mostert, C.W. Siyasiya, Phase transformation and microstructural control of the a-solidifying γ-Ti-45Al-2Nb-0.7Cr-0.3Si intermetallic alloy, J. Alloys Compd. 757 (2018) 8–15.
[6] S.T. Camagu, A.S. Bolokang, T.F.G. Muller, D.E. Motaung, C.J. Arendse, Surface characterization and formation mechanism of the ceramic $TiO_{2-x}N_x$ spherical powder induced by annealing in air, Powder Technol. 351 (2019) 229–237.
[7] A.S. Bolokang, D.E. Motaung, C.J. Arendse, T.F.G. Muller, Formation of the metastable FCC phase by ball milling and annealing of titanium–stearic acid powder, Adv. Powder Technol. 26 (2015) 632–639.
[8] S.-W. Kim, Y.M. Jeon, C.H. Park, J.H. Kim, D.-H. Kim, J.-T. Yeom, Martensitic phase transformation of TiNi thin films fabricated by co-sputtering deposition, J. Alloys Compd. 580 (2013) 5–9.
[9] Y. Hida, E. Chaieb, A. Derkaoui, A. Tahani, L. Elfarh, Pure titanium corrosion inhibition by heat treatment in 3M HCl solution: an electrochemical impedance spectroscopy (E.I.S) study, Mater. Today Proc. 13 (2019) 899–908.
[10] D. Li, K. Wang, Z. Yan, Y. Cao, R.D.K. Misra, R. Xin, Q. Liu, Evolution of microstructure and tensile properties during the three-stage heat treatment of TA19 titanium alloy, Mater. Sci. Eng., A 716 (2018) 157–164.
[11] S. Liu, Y.C. Shin, Additive manufacturing of Ti6Al4V alloy: a review, Mater. Des. 164 (2019), 107552.
[12] M.A. Surmeneva, R.A. Surmenev, E.A. Chudinova, A. Koptioug, M.S. Tkachev, S. N. Gorodzha, L.-E. Rännar, Fabrication of multiple-layered gradient cellular metal scaffold via electron beam melting for segmental bone reconstruction, Mater. Des. 133 (2017) 195–204.
[13] S. Wang, L. Liu, K. Li, L. Zhu, J. Chen, Y. Hao, Pore functionally graded Ti6Al4V scaffolds for bone tissue engineering application, Mater. Des. 168 (2019) 107643–107649.
[14] C. Chen, Y. Hao, X. Bai, J. Ni, S.-M. Chung, F. Liu, In-Seop Lee, 3D printed porous Ti6Al4V cage: effects of additive angle on surface properties and biocompatibility; bone ingrowth in Beagle tibia model, Mater. Des. 175 (2019) 107824–107831.
[15] S. Liu, Y.C. Shin, The influences ofmelting degree of TiC reinforcements on microstructure and mechanical properties of laser direct deposited Ti6Al4V-TiC composites, Mater. Des. 136 (2017) 185–195.
[16] C. Sutowo, A.A. Alhamidi, M.I.A. Basir, F. Rokhmanto, Effect of quenching medium on the microstructure of hot rolled Ti-6Al-6Nb alloy for medical application, AIP Conf. Proc. 1964 (2018), 020045, https://doi.org/10.1063/1.5038327.
[17] Z-f. Shi, H-z. Guo, J-y. Han, Z-k. Yao, Microstructure and mechanical properties of TC21 titanium alloy after heat treatment, Trans. Nonferrous Metals Soc. China 23 (2013) 2882–2889.
[18] R.N. Elshaer, K.M. Ibrahim, A.F. Barakat, R.R. Abbas, Effect of heat treatment processes on microstructure and mechanical behavior of TC21 titanium alloy, Open J. Met. 7 (2017) 39–57.
[19] D. Zhao, J. Fan, Z. Zhang, X. Liu, Q. Wang, Z. Chen, B. Tang, H. Kou, S. Jia, J. Li, Microstructure and texture variations in high temperature titanium alloy Ti65 sheets with direrent rolling modes and heat treatments, Materials 13 (2020) 2466, https://doi.org/10.3390/ma13112466.
[20] R. Julien, V. Velay, V. Vidal, Y. Dahan, R. Forestier, F. Rezai-Aria, Characterization and modeling of forged Ti-6Al-4V Titanium alloy with microstructural considerations during quenching process, Int. J. Mech. Sci. May 28 (2018). https://hal-mines-albi.archives-ouvertes.fr/hal-01799489.
[21] A.S. Bolokang, M.J. Phasha, D.E. Motaung, F.R. Cummings, T.F.G. Muller, C. J. Arendse, Microstructure and phase transformation on milled and unmilled Ti induced by water quenching, Mater. Lett. 132 (2014) 157–161.
[22] D. Stojakovic, Electron backscatter diffraction in materials characterization, Proc. Appl. Ceram. 6 (1) (2012) 1–13.
[23] Y. Li, J. Li, B.X. Liu, Homogeneous shear-driven reversible α'-to-α'' phase transformation and superelasticity of titanium investigated by molecular dynamics simulations, Acta Mater. 93 (2015) 105–113.
[24] C. Xu, G. He, C. Liu, H. Wang, Twin-size effects on the hardness and plastic deformation mechanisms of nanotwinned diamond, Ceram. Int. 44 (2018) 22121–22128.
[25] B.S. Parker, Blending of Powders for In-Situ Alloying of Ti-6Al-4V Laser Powder Bed Fusion, Thesis, Stellenbosch University, 2021, pp. 1–144, http://scholar.sun.ac.za.
[26] N. Bahlawane, D. Lenoble, Vanadium Oxide Compounds: Structure, Properties and Growth from Gas Phase, Chemical Vapour Deposition, 2014, pp. 299–311, https://doi.org/10.1002/cvde.201400057.
[27] J. Zhang, C.C. Tasan, M.J. Lai, A.-C. Dippel, D. Raabe, Complexion-mediated martensitic phase transformation in Titanium, Nat. Comput. 8 (14210) (2017) 1–8, https://doi.org/10.1038/ncomms14210. www.nature.com/naturecommunications.
[28] P. Tan, F. Shen, B. Li, K. Zhou, A thermo-metallurgical-mechanical model for selective laser melting of Ti6Al4V, Mater. Des. 168 (2019), 107642.
[29] F. Kong, Y. Chen, D. Zhang, Interfacial microstructure and shear strength of Ti–6Al–4V/TiAl laminate composite sheet fabricated by hot packed rolling, Mater. Des. 32 (2011) 3167–3172.
[30] R. German, Powder Metallurgy Science, Metal Powder Industry Federation, Princeton, New Jersey, USA, 1994, pp. 451–455.
[31] Y. Yang, Y.J. liu, J. Chen, H.L. Wang, Z.Q. Zhang, Y.J. Lu, S.Q. Wu, J.X. Lin, Crystallographic features of α variants and β phase for Ti-6Al-4V alloy fabricated by selective laser melting, Mater. Sci. Eng., A 707 (2017) 548–558.
[32] C.T. Kwok, P.K. Wong, F.T. Cheng, H.C. Man, Characterization and corrosion behavior of hydroxyapatite coatings on Ti6Al4V fabricated by electrophoretic deposition, Appl. Surf. Sci. 255 (2009) 6736–6744.
[33] Y. Xia, H. Dong, X. Hao, P. Li, S. Li, Vacuum brazing of Ti6Al4V alloy to 316L stainless steel using a Ti-Cu-based amorphous filler metal, J. Mater. Process. Technol. 269 (2019) 35–44.
[34] Z. Sun, F. Shuang, W. Ma, Investigations of vibration cutting mechanisms of Ti6Al4V alloy, Int. J. Mech.l Sci. 148 (2018) 510–530.
[35] M.E. Ramosoeu, H.K. Chikwanda, A.S. Bolokang, G. Booysen, T.N. Ngonda, Additive Manufacturing: Characterization of TI-6AI-4V Alloy Intended for Biomedical Application, The Southern African Institute of Mining and Metallurgy Advanced Metals Initiative, Light Metals Conference, 2010, pp. 337–344.
[36] R. Wauthle, B. Vrancken, B. Beynaerts, K.J.J. Schrooten, J.-P. Kruth, J. V. Humbeeck, Effects of build orientation and heat treatment on the microstructure

andmechanical properties of selective laser melted Ti6Al4V lattice structures, Addit. Manuf. 5 (2015) 77–84.
[37] C. Zhang, H. Zhu, H. Liao, Y. Cheng, Z. Hu, X. Zeng, Effect of heat treatments on fatigue property of selective laser melting AlSi10Mg, Int. J. Fatig. 116 (2018) 513–522.
[38] V. Cain, L. Thijs, J. Van Humbeeck, B. Van Hooreweder, R. Knutsen, Crack propagation and fracture toughness of Ti6Al4V alloy produced byselective laser melting, Addit. Manuf. 5 (2015) 68–76.
[39] A.M. Vilardell, G. Fredriksson, I. Yadroitsev, P. Krakhmalev, Fracture mechanisms in the as-built and stress-relieved laser powder bed fusion Ti6Al4V ELI alloy, Opt Laser. Technol. 109 (2019) 608–615.
[40] H. Ali, H. Ghadbeigi, K. Mumtaz, Effect of scanning strategies on residual stress and mechanical properties of Selective Laser Melted Ti6Al4V, Mater. Sci. Eng., A 712 (2018) 175–187.
[41] J.D. Roehling, W.L. Smith, T.T. Roehling, B. Vrancken, G.M. Guss, J.T. McKeown, M.R. Hill, M.J. Matthews, Reducing residual stress by selective large-area diode surface heating during laser powder bed fusion additive manufacturing, Addit. Manuf. 28 (2019) 228–235.
[42] S.-H. Hsu, Y.-H. Ho, M.-X. Ho, J.-C. Wang, C. Pan, Corrigendum to “On the formation of vapor film during quenching in de-ionized water and elimination of film boiling during quenching in natural sea water’’, Int. J. Heat Mass Tran. 86 (2015) 65–71.
[43] A. Ferrari, D.G. Sangiovanni, J. Rogal, R. Drautz, First principles characterization of reversible martensitic transformations, Phys. Rev. B 99 (2019), 094107-1-094107-6.
[44] A.S. Bolokang, M.J. Phasha, Thermal analysis on the curie temperature of nanocrystalline Ni produced by ball milling, Adv. Powder Technol. 22 (2011) 518–521.
[45] A.S. Bolokang, M.J. Phasha, Solid-state transformation in ball milled nickel powder, Mater. Lett. 64 (2010) 1894–1897.
[46] H. Shahmir, T.G. Langdon, An evaluation of the hexagonal close-packed to face-centered cubic phase transformation in a Ti-6Al-4V alloy during high-pressure torsion, Mater. Sci. Eng., A 704 (2017) 212–217.
[47] Y.G. Liu, M.Q. Li, H.J. Liu, Deformation induced face-centered cubic titanium and its twinning behavior in Ti–6Al–4V, Scripta Mater. 119 (2016) 5–8.
[48] N. Ao, D. Liu, C. Liu, X. Zhang, D. Liu, Face-centered titanium induced by ultrasonic surface rolling process in Ti-6Al-4V alloy and its tensile behaviour, Mater. Char. 145 (2018) 527–533.
[49] A.S. Bolokang, M.N. Mathabathe, S. Chikosha, D.E. Motaung, Investigating the heat resistant properties of the TiNi shape memory alloy on the B19′→B2 phase transformation using the alloy powder, Surface. Interfac. 20 (2020), 100608.
[50] H. Matsumoto, K. Yoshida, S.H. Lee, Y. Ono, A. Chiba, Mater. Lett. 98 (2013) 209–212.
[51] P. Kumar, O. Prakash, U. Ramamurty, Microstructural optimization through heat treatment for enhancing the fracture toughness and fatigue crack growth resistance of selective laser melted Tie6Ale4V alloy, Acta Mater. 169 (2019) 45–59.
[52] Z. Tarzimoghadam, S. Sandlöbes, K.G. Pradeep, D. Raabe, Microstructure design and mechanical properties in a near-a Ti–4Mo alloy, Acta Mater. 97 (2015) 291–304.
[53] S. Sandlobes, S. Korte-Kerzel, D. Raabe, On the influence of the heat treatment on microstructure formation and mechanical properties of near-α Ti-Fe alloys, Mater. Sci. Eng., A 748 (2019) 301–312.